ENCIT 2018

ABCM Associação Brasileira de Engenharia e Ciências Mecânicas

17th Brazilian Congress of Thermal Sciences and Engineering
November 25th-28th, 2018, Águas de Lindóia, SP, Brazil

ENCIT-2018-0677
INFLUENCE OF CURVATURE VARIATION ON THE SECONDARY INSTABILITIES

L. F. Marques
J. K. Rogenski
L. F. Souza
University of São Paulo, Av. Trabalhador São Carlense, 400, São Carlos, Brazil
larapomac@gmail.com, josuelkr@gmail.com, lefraso@gmail.com

Abstract. *The centrifugal instability mechanism of boundary layers over concave surfaces is responsible for the development of counter-rotating vortices aligned in the streamwise direction known as Görtler vortices. Depending on various geometrical and flow conditions, these vortices in its nonlinear form can significantly distort the baseline flow and lead to secondary instabilities. These disturbances can develop into horseshoe vortices or a sinuous motion of the Görtler vortices, known as even (varicose) and odd (sinuous) modes, respectively. In the present study, numerical simulations have been performed using a high-order, pseudo-spectral numerical code to investigate the influence of the curvature variation on the secondary instabilities. Considering a surface with variable curvature and a full concave plate, one spanwise wavelength was disturbed to compare the nonlinear evolution of Görtler vortices. Multi-frequency unsteady disturbances are introduced with the same spanwise wavelength as the Görtler vortices, but with two different spanwise phases are used to analyze their effects on the secondary instability. A comparative analysis of the evolution of nonstationary disturbances to different curvature distribution shows that for the spanwise wavelength analyzed, the odd modes grow first and dominate the transition process. Besides that, results provide evidence that curvature has a strong influence on this growth.*

Keywords:*Numerical Simulation, Görtler vortices, Secondary instabilities, curvature variation*

1. INTRODUCTION

Some of the greatest problems in fluid mechanics is the prediction of transition in boundary layers on curved surfaces. This has long been the subject of intense research, and yet today uncertainty and a lack of consensus about the location of transition onset still remaining. The nonlinear growth of longitudinal vortices in a boundary layer on curved surfaces is a relevant topic in fluid mechanics because these vortices appear in several technological applications. When considering turbomachineries, for example, the Reynolds number may be fairly low and the stability of the laminar flow might be a prime factor in determining the efficiency of this application.

It is known that in boundary layers developed over concave walls laminar-turbulent transition phenomenon may occur. This instability mechanism may lead to the formation of a system of streamwise, counter-rotating vortex pairs known as Görtler vortices. These vortices under certain conditions can be efficient precursors to transition. They grow at a certain rate, depending on the surface curvature and the receptivity of the boundary layer to environmental disturbances and surface imperfections. In boundary layers over surfaces having small to medium curvature, Görtler vortices can significantly alter the mean flow and cause the laminar flow to break down into turbulence (Görtler, 1941).

Different approaches related to this subject have been presented. Otto and Denier (1994) analyzed, via a nonlocal linear stability analysis, the effect of cross-flow and pressure gradient on Görtler vortices developing along a concave wall of constant radius of curvature. Numerical studies related to Görtler instability considering curvature variations are very scarce. Benmalek and Saric (1994) studied numerically the effects of curvature on the growth of counter-rotating streamwise vortices, generated on the concave section of a variable curvature wall via the Görtler instability mechanism. In the experimental study conducted by Zhang *et al.* (1995), the energy metric was adopted to verify the Görtler development on concave surfaces with $2.0\ m$ of radius of curvature. With this metric is possible to analyze the amplification rate from the eigenvalue problem.

A comprehensive review of the structure of secondary flows in turbine cascades has been given by Sieverding (1985). Some experimental information about secondary flow from visualization studies is provided by Sonoda (1985), Goldstein and Spores (1988), Joslyn and Dring (1990) and Jabbari *et al.* (1992). A few years later, the secondary instability of Görtler vortices was investigated by Bottaro and Klingmann (1996) through a linear model based on a Floquet-type analysis. They considered the experimental conditions of Swearingen and Blackwelder (1987), leading initially to a sinuous secondary instability independent of the spanwise wavenumber. Further downstream several modes became unstable and for large spanwise wavenumber, the varicose mode dominated. They also analyzed the effect of Reynolds

number and boundary layer growth concluding that the secondary instability is mainly inviscid and the flow may be considered parallel, consistent with the large growth rate found for the secondary instability modes. Girgis and Liu (2002) studied the nonlinear development of the sinuous mode and discussed the effect of Görtler vortices and the resulting secondary instability on a mixing layer flow. Their results confirm previous results regarding the relationship between the varicose mode and the streamwise velocity gradients in the wall-normal direction, while the sinuous mode correlates well with the spanwise gradients of the streamwise velocity.

In a recent paper, Souza (2017) investigate the secondary instability of Görtler flow using high-order spatial numerical simulation. Three different spanwise phases were used and the effect on the secondary instability was analyzed. In this study, both, even and odd secondary instabilities were observed, according to the relative spanwise position of the unsteady disturbances.

Therefore, in order to enrich the available literature and to better highlight the transition mechanism, the present study aims to investigate the effects of the curvature variation on the Secondary instabilities using a nonlinear numerical simulation code. This study includes an analysis in which one spanwise wavelength, $\lambda^* = 8.674 \times 10^{-4}\ m$, was disturbed when submitted to concave plates with different radius distributions.

2. PROBLEM FORMULATION

Secondary instabilities analyze is done considering a mean-flow state represented by a two-dimensional boundary layer flow over two different curvature distributions. We consider the flow on the pressure side of a turbine blade adopted in the experimental study (Wang *et al.*, 1997). We take the minimum radius of this geometry to define a fully concave plate. The radius distribution of the considered curvatures and the local Görtler number were been displayed in Fig. 1, where cc and vc mean constant curvature and variable curvature, respectively. For the variable curvature, the local Görtler number reaches a maximum value corresponding to 18.13 at $x = 5.88$ and decreases with the increase in the radius of the blade.

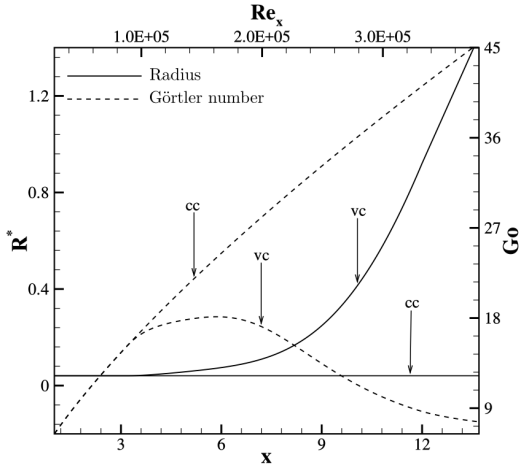

Figure 1. Radius distribution and Görtler number to a constant curvature (cc) and a variable curvature (vc)

The problem is modeled through a Navier-Stokes system of equations written in vorticity-velocity formulation. We assume that vorticity and velocity components are the superposition of a base flow and a disturbance represented by

$$\widetilde{g} = g_b + g,$$

where $\widetilde{g} = \{\widetilde{u}, \widetilde{v}, \widetilde{w}, \widetilde{\omega}_x, \widetilde{\omega}_y, \widetilde{\omega}_z\}$ corresponds to the total amounts of velocity and vorticity components, g_b denotes the base flow and the disturbance is represented by g. In this formulation the linear and nonlinear terms can be isolated. This facilitates stability analysis of any base flow.

Assuming that U^*_∞ is the potential streamwise velocity at a L^* position from the leading edge and dimensional quantities are identified by an asterisk, non-dimensionalization relations hold for

$$x = \frac{x^*}{L^*},\ \ y = \frac{y^*}{L^*},\ \ z = \frac{z^*}{L^*},$$

$$u = \frac{u^*}{U^*_\infty},\ \ v = \frac{v^*}{U^*_\infty},\ \ w = \frac{w^*}{U^*_\infty},$$

$$\omega_x = \frac{\omega^*_x L^*}{U^*_\infty},\ \ \omega_y = \frac{\omega^*_y L^*}{U^*_\infty},\ \ \omega_z = \frac{\omega^*_z L^*}{U^*_\infty}.$$

The field equations to the base flow consist of the vorticity transport equation

$$\frac{\partial}{\partial x}\left(u_b\omega_{zb}\right)+\frac{\partial}{\partial y}(v_b\omega_{zb})=\frac{1}{Re}\left(\frac{\partial^2\omega_{zb}}{\partial x^2}+\frac{\partial^2\omega_{zb}}{\partial y^2}\right),$$

the Poisson equation for the normal-to-the-wall velocity component

$$\frac{\partial^2 v_b}{\partial x^2}+\frac{\partial^2 v_b}{\partial y^2}=-\frac{\partial\omega_{zb}}{\partial x},$$

and the continuity equation

$$\frac{\partial^2 u_b}{\partial x^2}=-\frac{\partial^2 v_b}{\partial x\partial y},$$

and these equations are solved in a rectangular computational domain bounded by the wall, a potential flow far away from the wall, and the inflow (left) and outflow (right) boundaries. The no-slip and no-penetration conditions are imposed at the wall. These conditions consist of $u_b=0$, $v_b=0$, $\frac{\partial v_b}{\partial y}|_{x,y}=0$, $\frac{\partial\omega_b}{\partial x}|_{x,y=0}=-\frac{\partial^2 v_b}{\partial y^2}|_{x,y=0}$. The inflow conditions consist of specifying u_b $(x=x_0,y)$, v_b $(x=x_0,y)$, ω_{zb} $(x=x_0,y)$, where x_0 denotes the location of the inflow boundary. In the analysis, we have specified the inflow conditions on the basis of the solution of the Blasius equation (Schlichting, 1979). Far away from the wall, the flow assumes a potential form which leads to $\omega_{zb}(x,y=y_{max})=0$ and permits an arbitrary specification of $u_b(x,y=y_{max})=U_\infty$. The continuity equation is used to determine v_b from the known U_∞. Outflow boundary conditions have the form $\frac{\partial^2 u_b}{\partial x^2}|_{x=x_{max},y}=\frac{\partial^2 v_b}{\partial x^2}|_{x=x_{max},y}=\frac{\partial^2\omega_{zb}}{\partial x^2}|_{x=x_{max},y}=0$, where x_{max} denotes the location of the outflow boundary.

We consider as relevant nondimensional parameters the Re, Go, and Λ, known as Reynolds and Görtler numbers, and wavelength parameter defined respectively by

$$Re=\frac{U_\infty^* L^*}{\nu^*},\;\; Go=Re^{\frac{1}{4}}\sqrt{\frac{L^*}{R^*}},\;\; \Lambda=\frac{U_\infty^*\lambda^*}{\nu^*}\sqrt{\frac{\lambda^*}{R^*}},$$

where ν^* denotes the kinematic viscosity. The curvature radius of the concave surface is represented by R^* and λ^* denotes the spanwise wavelength.

Defining the vorticity as the negative curl of the velocity, and using the fact that both, the velocity and the vorticity fields are solenoidal, we obtain the three-dimensional form of the vorticity transport equation (Souza *et al.*, 2004) :

$$\frac{\partial\omega_x}{\partial t}+\frac{\partial a}{\partial y}-\frac{\partial b}{\partial z}+\frac{Go^2}{\sqrt{Re}}\frac{\partial d}{\partial z} = \frac{1}{Re}\nabla^2\omega_x, \tag{1}$$

$$\frac{\partial\omega_y}{\partial t}+\frac{\partial c}{\partial z}-\frac{\partial a}{\partial x} = \frac{1}{Re}\nabla^2\omega_y, \tag{2}$$

$$\frac{\partial\omega_z}{\partial t}+\frac{\partial b}{\partial x}-\frac{\partial c}{\partial y}-\frac{\partial}{\partial x}\frac{Go^2 d}{\sqrt{Re}} = \frac{1}{Re}\nabla^2\omega_z. \tag{3}$$

The linear terms a, b, c and d shown in Eqs. (1) – (3) are defined by

$$\begin{aligned} a &= \omega_x(v_b+v)-\omega_y(u_b+u),\\ b &= \omega_{zb}u+\omega_z(u_b+u)-\omega_x w,\\ c &= (w_b+w)\omega_y-(v_b+v)\omega_z-\omega_{zb}v,\\ d &= 2u_b u+u^2, \end{aligned}$$

where the derivative of d captures the curvature effects.

The continuity equation is given by

$$\frac{\partial u}{\partial x}+\frac{\partial v}{\partial y}+\frac{\partial w}{\partial z} = 0. \tag{4}$$

From the definition of vorticity and the mass conservation equation, we obtain Poisson equations for each velocity component:

$$\frac{\partial^2 u}{\partial x^2}+\frac{\partial^2 u}{\partial z^2} = -\frac{\partial\omega_y}{\partial z}-\frac{\partial^2 v}{\partial x\partial y}, \tag{5}$$

$$\frac{\partial^2 v}{\partial x^2}+\frac{\partial^2 v}{\partial y^2}+\frac{\partial^2 v}{\partial z^2} = -\frac{\partial\omega_z}{\partial x}+\frac{\partial\omega_x}{\partial z}, \tag{6}$$

$$\frac{\partial^2 w}{\partial x^2}+\frac{\partial^2 w}{\partial z^2} = \frac{\partial\omega_y}{\partial x}-\frac{\partial^2 v}{\partial y\partial z}. \tag{7}$$

Therefore, Eqs. (1) – (3), (4) and (5) – (7) define the system of equations for disturbances. The necessary boundary conditions to close this system of equations can be found in (Vinicius *et al.*, 2013).

3. NUMERICAL METHOD

The geometry of the numerical domain is sketched in Fig. 2, and the numerical method used to solve the system of the governing equations is based on high order compact finite difference approximations for the discretization of the streamwise and wall-normal spatial derivatives (Petri *et al.*, 2015). The time integration was carried out by a classical fourth order Runge-Kutta scheme. A buffer-domain technique was considered to avoid reflection of disturbances at the boundaries.

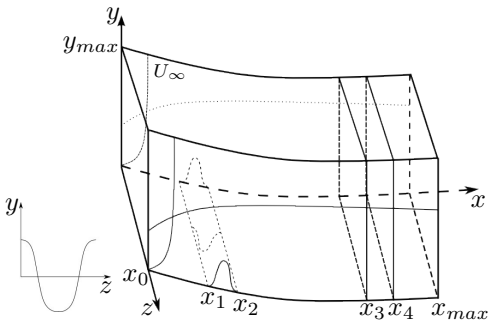

Figure 2. Sketch of the numerical domain

Assuming that there is periodicity in the spanwise direction of the flow we adopted a spectral method. Each total amounts of velocity and vorticity components denoted by g, can be written as a linear combination of the $k+1$ spanwise Fourier modes

$$g(x,y,z,t) = \sum_{k=0}^{K} g_k(x,y,t) e^{-\iota k \beta z}, \tag{8}$$

where ι is the imaginary unit, β denotes the spanwise wavenumber and it is given by $\beta = \dfrac{2\pi}{\lambda}$. Substituting the Fourier transforms given by Eq. (8) in the Eqs. (1) – (3) and (5) – (7), one obtains the governing equations in the Fourier space:

$$\frac{\partial \omega_{x_k}}{\partial t} + \frac{\partial a_k}{\partial y} + \iota k\beta b_k - \iota k\beta d_k \frac{Go^2}{\sqrt{Re}} = \frac{1}{Re}\nabla_k^2 \omega_{x_k}, \tag{9}$$

$$\frac{\partial \omega_{y_k}}{\partial t} - \iota k\beta c_k - \frac{\partial a_k}{\partial x} = \frac{1}{Re}\nabla_k^2 \omega_{y_k}, \tag{10}$$

$$\frac{\partial \omega_{z_k}}{\partial t} + \frac{\partial b_k}{\partial x} - \frac{\partial c_k}{\partial y} - \frac{\partial d_k}{\partial x}\frac{Go^2}{\sqrt{Re}} = \frac{1}{Re}\nabla_k^2 \omega_{z_k}, \tag{11}$$

$$\frac{\partial^2 u_k}{\partial x^2} - k^2\beta^2 u_k = -\iota k\beta \omega_{y_k} - \frac{\partial^2 v_k}{\partial x \partial y}, \tag{12}$$

$$\frac{\partial^2 v_k}{\partial x^2} + \frac{\partial^2 v_k}{\partial y^2} - k^2\beta^2 v_k = -\frac{\partial \omega_{z_k}}{\partial x} - \iota\beta\omega_{x_k}, \tag{13}$$

$$\frac{\partial^2 w_k}{\partial x^2} - k^2\beta^2 w_k = \frac{\partial \omega_{y_k}}{\partial x} + \iota k\beta \frac{\partial v_k}{\partial y}, \tag{14}$$

where $\nabla_k^2 = \left(\frac{\partial^2}{\partial x^2} + \frac{\partial^2}{\partial y^2} - k^2\beta^2\right)$.

The linear coupled system of equations given by Eqs. (9) – (14) is solved numerically in the domain shown schematically in Fig. 2. The inflow boundary is represented by $x = x_0$ and the outflow boundary, $x = x_{max}$. Disturbances are introduced into the flow field using spanwise suction and blowing of mass at the wall in a disturbance strip at the wall located in the region between points x_1 and x_2. In order to avoid wave reflections at the outflow boundary, we implemented in the region located between x_3 and x_4 a buffer domain technique (Kloker *et al.*, 1993). The calculation of spatial derivatives was done using a high order compact finite difference-schemes (Souza *et al.*, 2005). The v-Poisson equation, defined in Eq. (13), was solved using a multigrid Full Approximation Scheme (FAS) (Stüben and Trottenberg, 1981). For the implementation, we adopted a V-cycle working with four levels. The solution will converge, ie, the steady state is reached when the maximum difference between the $k = 1$ spanwise vorticity component is smaller than a given considerably small parameter in two consecutive time steps.

4. RESULTS

Nonlinear simulations have been conducted considering the same physical parameters of the experiment of Wang *et al.* (1997). The pressure side of the experimental turbine blade profile was adapted according to the computational domain

considered in the present study. The free stream velocity at $x^* = L = 1.0 \times 10^{-2}\ m$ is $U^*_\infty = 41.806\ ms^{-1}$ and the corresponding Reynolds number is $Re = 2.7704 \times 10^4$, the kinematic viscosity $\nu^* = 1.5 \times 10^{-5}\ m^2 s^{-1}$, the time step $dt = 2 \times 10^{-1} \times dx$, the number of points in the x and y directions are 2265 and 257, respectively. The distance between two consecutive points in the x and y directions are $dx = 6.23 \times 10^{-3}$ and $dy = 5.0 \times 10^{-4}$. The disturbances were introduced in the region $1.53 \leq x \leq 1.99$, with a small amplitude of $A = 1 \times 10^{-6}$. A stretching factor of 1% is adopted in the y-direction.

4.1 Görtler Instability

The resulting flow field with Görtler vortices was used as initial condition in the secondary instability simulations. Figure 3 shows the streamwise development of the disturbance energy for each Fourier mode k, from 0 to 22, for two different radius distribution: constant curvature (Fig. 3(a)), and variable curvature (Fig. 3(b)). The energy of each Fourier mode is quantified by the integral measures $E_k(x) = \int_0^\infty |u_k|^2\, dy,\ 0 \leq k \leq K-1$ (Benmalek and Saric, 1994). Observe that at inflow where the curvature of the wall has a constant radius for both wall cases studied, the energy of the Görtler vortices grow linearly. Further, downstream nonlinear effects become more significant, and to constant curvature case

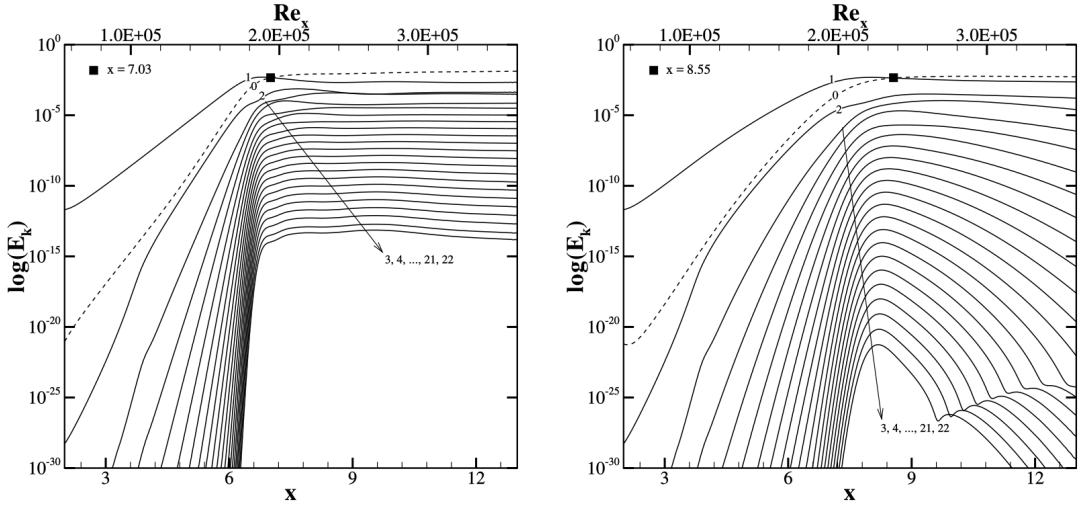

(a) Constant curvature (b) Variable curvature

Figure 3. Streamwise development of the disturbance energy of each Fourier mode for $\lambda^* = 8.674 \times 10^{-4}\ m$. Comparison between constant curvature and variable curvature plates. Fourier modes from 0 to 22. Black squares identify the position where the energy of the modes $k = 0$ and $k = 1$ are equal

(Fig. 3(a)) saturation starts at $x = 7.03$. In the saturation region, the difference between the amplitude of consecutive modes are almost constant, and the amplitudes of the last modes are very small. In Fig. 3(b), the energy of each mode

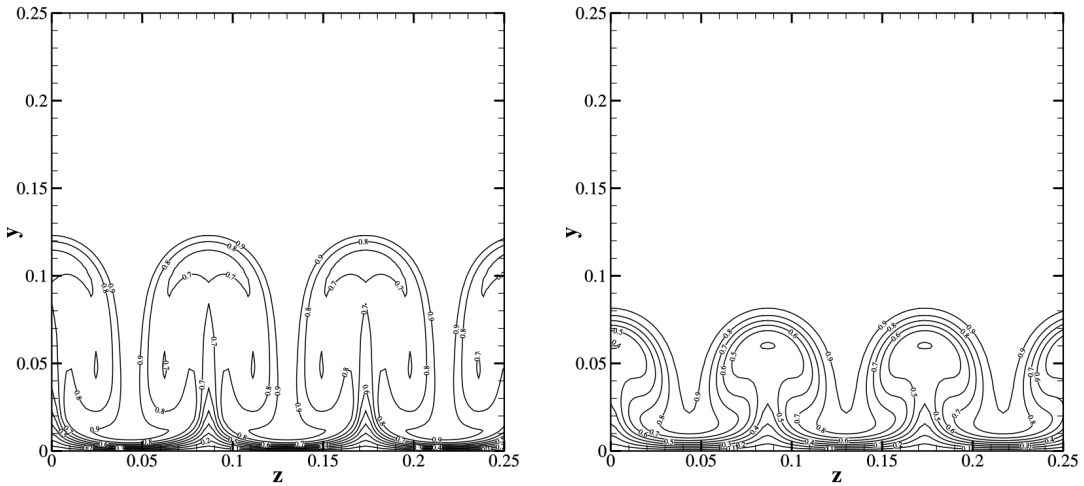

(a) Constant curvature (b) Variable curvature

Figure 4. Distributions of u-velocity component in the (z, y)-plane for vortices with $\lambda_z = 8.674 \times 10^{-4}\ m$ at streamwise positions $x = 8.47$. Isolines from 0.1 to 0.9 in steps of 0.1

is provided for the pressure side of a turbine blade case. In this case, one may notice that energy behavior is consistent with the fully concave case in the constant region. After radius curvature changing it is possible to see a decrease of amplitudes, which leads us to conclude that the centrifugal effects are turned off. However the higher the nonlinearities associated with the saturation of the Görtler vortices the lower the observed reduction in the energy modes (please see Fig. 3(b)). This fact suggests saturation as a natural streamwise limit in cases where curvature changes are considered to control the instability.

Figure 4 displays the isovelocity distribution in a crosscut at $x = 8.47$. The mushroom structure typical for Görtler flow can be observed in Fig. 4(a) and Fig. 4(b). In this streamwise position, the vortices are saturated, which means that the nonlinear effects become predominant.

4.2 Secondary Instability

The transition of the saturated steady flow is caused by unsteady disturbances. Therefore, the steady saturated flow with vortices has been combined with periodically pulsed low-amplitude disturbances to simulate the natural disturbance background. The periodic background pulse consists of harmonic waves with discrete frequencies from 200 Hz to 3200 Hz in steps of 200 Hz. The unsteady disturbances were introduced with the same modulation in the spanwise direction of the steady disturbance adopted to generate the Görtler vortices - $k = 1$. Two configurations are tested, each considering a different spanwise phase between the vortices and the unsteady disturbance. These configurations are illustrated in Fig. 5 (adapted from Souza (2017)), where the steady disturbance is shown as continuous line. The unsteady disturbances are shown as dashed and dotted lines, showing that they oscillate between the two lines, because they are standing waves in spanwise direction.

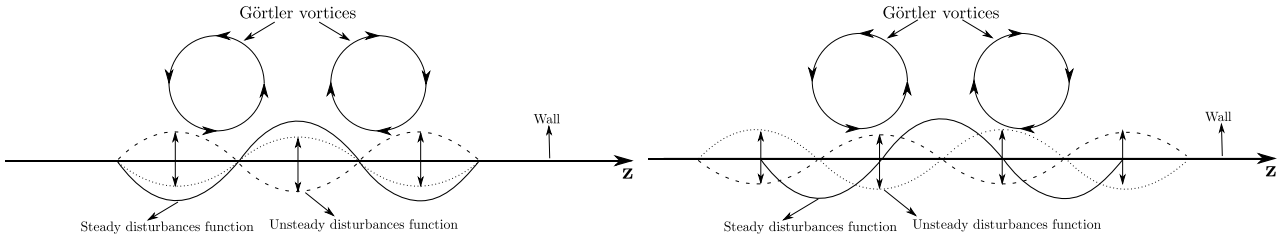

Figure 5. Spanwise distribution of the steady and unsteady disturbances and the position of the vortex. Two different spanwise distribution of the unsteady disturbances: (a) in phase with the vortex, and (b) phase shift of 90^o with the vortex

For the results presented in this section, disturbances introduced in phase eith Görtler vortices are represented by $A = 1.0 \times 10^{-5} + 0\iota$, and disturbances lagged at 90^o are represented by $A = 0 + 1.0 \times 10^{-5}\iota$. The introduction of the unsteady disturbances is done also via suction and blowing at the wall in three streamwise region $x:\ [5.88, 6.14]$, $[6.38, 6.64]$ and $[6.84, 7.1]$.

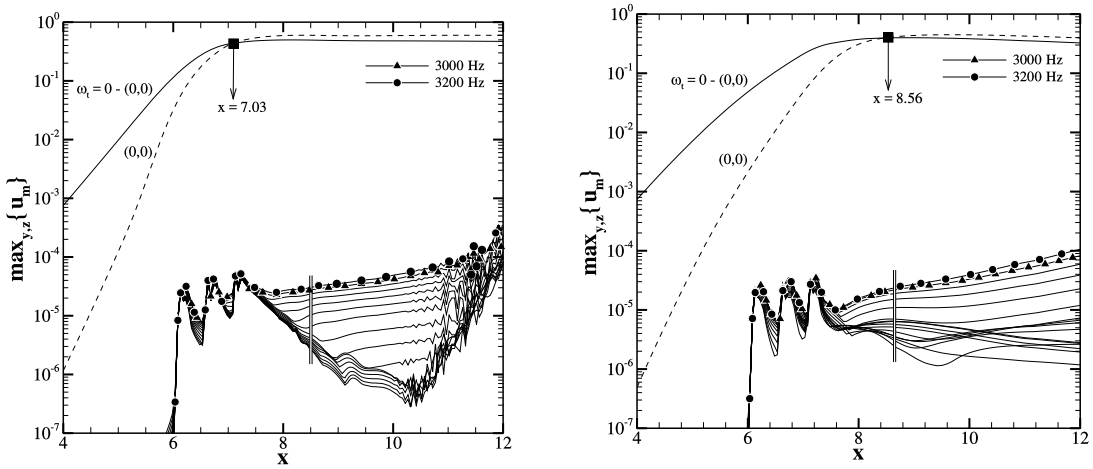

(a) Constant curvature (b) Variable curvature

Figure 6. Downstream amplitude development of Görtler vortex mode plus periodic background pulses. The unsteady disturbances were introduced with the same spanwise modulation and position of the vortex disturbance

Figure 6 and 7 show the maximum amplitude of the streamwise disturbance velocity u of each frequency over (z, y) plane in the streamwise direction. For the first analysis, disturbances were introduced with the same spanwise modu-

lation and position of the Görtler vortices. Figure 7 displays results to unsteady disturbances with a phase shift in the spanwise direction of 90^o to the vortex disturbance. In this figures the curves denoted by $(0, 0)$ represents the two-dimensional mean-flow distortion, and the curve denoted by $\omega_t = 0 - (0, 0)$ represents the three-dimensional part of it. Initially, it is possible to identify the existence of interaction between the wave packets and the base flow. In the region where the disturbance-generating packets were inserted it is observed that the behavior of the low and high-frequency disturbances presents a small difference, where a low-frequency disturbance decays/grows more slowly as compared to a high-frequency disturbance. This behavior evidences that the process that takes the flow from a primary stage to a secondary stage is conducted by the amplification of high frequencies.

For the case illustrated in Fig. 6 all modes exhibit a stable behavior in the region close to where they are introduced. For both curvature distributions, one significant decay of the low-frequency modes is observed, in which this drop is more abrupt to constant curvature (see Fig. 6(a)). For this case, the highest frequencies do not show a significant growth, remaining constant in the region defined by $7.76 \leq x \leq 11.25$. At $x \geq 10.2$, there is a change in the behavior of the low-frequency modes, where these modes present a significant amplification, competing with the high-frequency modes. This behavior is identified in a region dominated by secondary instability. It can also be observed that the mode with the highest growth rate corresponds to 3000 Hz.

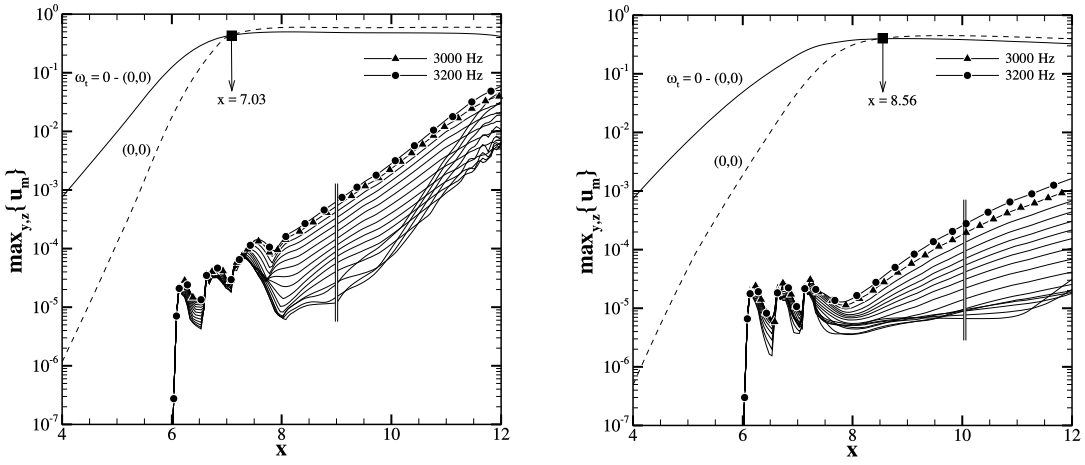

(a) Constant curvature (b) Variable curvature

Figure 7. Downstream amplitude development of Görtler vortex mode plus periodic background pulses. The unsteady disturbances were introduced with the same modulation, but with a phase shift in the spanwise direction of 90^o to the vortex disturbance

In Fig. 7 it is possible to see all unsteady disturbances start to decay in the region close to where they are introduced. After that, the disturbances of different frequencies start to amplify, in a region dominated by secondary instabilities. This behavior can be identified in both curvature distributions, but this growth is most significant in the case presented in Fig. 7(a) where all frequencies begin to be exponentially amplified at $x \geq 8$. In a region close to outflow, a competition between the highest and lowest frequency temporal modes is observed. The frequency with the higher values of growth rates in the secondary instability region to the constant and variable curvature corresponds to 3200 Hz.

The vortical structures in the instantaneous flow are visualized by Q isosurfaces to allow the identification of coherent vortices. Figure 8 shows Q isosurfaces with a value of $Q = 0.1$ considering two different curvature radius distributions. Even secondary-mode instability is presented in Fig. 8(a) (constant curvature) and Fig. 8(b) (variable curvature). Varicose-like structures may be observed at Fig. 8(a) in a region where $x \geq 12.5$. In this region, the horseshoe structures typical of even secondary-mode instability can be clearly seen. Figure 9(a) (constant curvature) and Fig. 9(b) (variable curvature) show the odd secondary-mode instability. In Fig. 9(a) the sinuous-type structures are well characterized in the range of $12.75 \leq x \leq 13.75$. For the region where $x \geq 13.75$, the process of visualization of the flow becomes increasingly difficult due to the complexity of the associated vortical structures. Note that by taking a boundary layer flow on the pressure side of a turbine blade (Fig. 8(b) and Fig. 9(b)), none of the types of secondary instabilities investigated were observed.

5. CONCLUSIONS

In the present study the influence of the curvature radius distributions on secondary instabilities, sinuous and varicose types, was investigated by means of high-order numerical simulations. The secondary instability was excited by the introduction of low-amplitude unsteady, time-periodic, disturbance pulses. Unsteady frequencies were introduced range from 200 Hz to 3200 Hz in steps of 200 Hz. The dominating secondary instability mode, odd or even, could be achieved

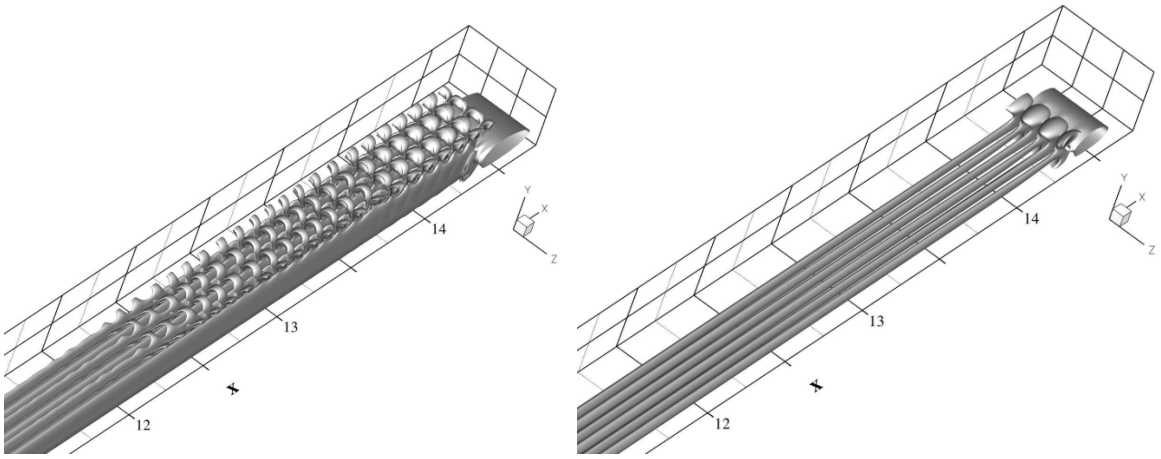

(a) Constant curvature (b) Variable curvature

Figure 8. Isosurfaces $Q = 0.1$ visualization of vortical structures in the instantaneous flow field. Görtler-vortex-mode plus periodic background pulses. The unsteady disturbances were introduced in phase with the vortex disturbance

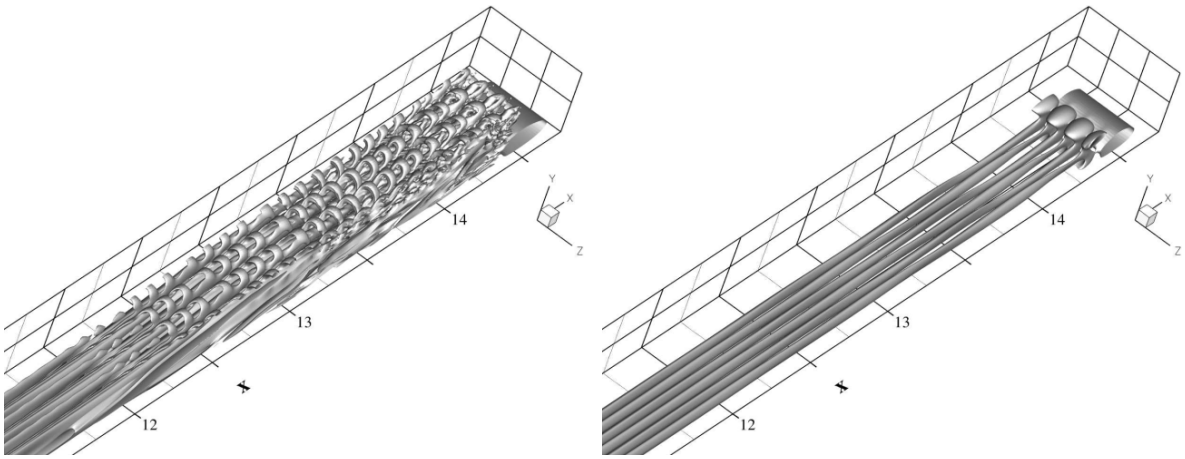

(a) Constant curvature (b) Variable curvature

Figure 9. Isosurfaces $Q = 0.1$ visualization of vortical structures in the instantaneous flow field. Görtler-vortex-mode plus periodic background pulses. The unsteady disturbances were introduced with a phase shift in the spanwise direction of 90^o to the vortex disturbance

depending on the curvature adopted. The in-phase configuration is found to excite even modes, whereas the phase shift of 90^o is found to excite odd modes. These results show that odd or even modes can be obtained in Görtler flow, depending on the geometries where the unsteady disturbances are introduced. With the present investigation it is possible to conclude that the curvature has a strong influence on the process of laminar-turbulent transition since when considering the pressure side of a turbine blade, secondary instabilities were not reached.

6. ACKNOWLEDGEMENTS

We thank CAPES for financial support and ICMC-USP for technical support and infrastructure. Research carried out using the computational resource of the Center for Mathematical Applied to Industry (CeMEAI) funded by FAPESP (Process Number #2013/07375-0).

7. REFERENCES

Benmalek, A. and Saric, W.S., 1994. "Effects of curvature variation on the nonlinear evolution of Goertler vortices". *Physics of Fluids*, Vol. 6, pp. 3353–3367.

Bottaro, A. and Klingmann, B., 1996. "On the linear breakdown of görtler vortices". *Eur. J. Mech. B / Fluids*, Vol. 15, pp. 301–330.

Girgis, I. and Liu, J., 2002. "Mixing enhancement via the release of strongly nonlinear longitudinal gÃűrtler vortices and their secondary instabilities into the mixing region". *J. Fluid Mech.*, Vol. 468, pp. 29–75.

Goldstein, R. and Spores, R., 1988. "Turbulent transport on the endwall in the region between adjacent turbine blades". *ASME Journal of Heat Transfer*, Vol. 110, pp. 862–869.

Görtler, H., 1941. "Instabilita-umt laminarer Grenzchichten an Konkaven Wanden gegenber gewissen dreidimensionalen Storungen". *ZAMM*, Vol. 5, pp. 250–252.

Jabbari, M., Goldstein, R., Marston, K. and Eckert, E., 1992. "Three dimensional flow at the junction between a turbine blade and endwall". *Warme- and Stoffubertragung*, Vol. 27, pp. 51–59.

Joslyn, D. and Dring, R., 1990. "Three-dimensional flow in an axial turbine: Part 1-aerodynamic mechanisms". *ASME paper, 90-GT-56*.

Kloker, M., Konzelmann, U. and Fasel, H., 1993. "Outflow boundary conditions for spatial Navier-Stokes simulations in transition boundary layers". *AIAA Journal*, Vol. 31, pp. 620–628.

Otto, S. and Denier, J., 1994. "The Effect of Crossflow on Görtler Vortices". *Final Report Institute for Computer Applications in Science and Engineering, Hampton, VA*.

Petri, L., Sartori, P., Rogenski, J.K. and Souza, L.F., 2015. "Verification and validation of a Direct Numerical Simulation code". *Computer methods in applied mechanics and engineering*, Vol. 291, pp. 266–279.

Schlichting, H., 1979. *Boundary-Layer Theory*. McGraw-Hill, IncH.

Sieverding, C., 1985. "Recent progress in the understanding of basic aspects of secondary flows in turbine blade passages". *ASME Journal of Engineering for Gas Turbine and Power*, Vol. 107, pp. 248–257.

Sonoda, T., 1985. "Experimental investigation on spatial development of streamwise vortices in a turbine inlet guide vane cascade". *AASME paper, 85-GT-20*.

Souza, L.F., Mendonça, M.T., de Medeiros, M.A.F. and Kloker, M., 2004. "Seeding of Görtler Vortices Through a Suction and Blowing Strip". *Journal of the Brazilian Society of Mechanical Sciences*, Vol. XXVI, pp. 269–279.

Souza, L.F., Mendonça, M.T. and Medeiros, M.A.F., 2005. "The advantages of using high-order finite differences schemes in laminar-turbulent transition studies". *International Journal for Numerical Methods in Fluids*, Vol. 48, pp. 565–592.

Souza, L.F., 2017. "On the odd and even secondary instabilities of görtler vortices". *Theoretical and Computational Fluid Dynamics*, Vol. 31, pp. 405–425.

Stüben, K. and Trottenberg, U., 1981. *Nonlinear multigrid methods, the full approximation scheme*, Köln-Porz, chapter 5, pp. 58–71. Lecture Notes in Mathematics.

Swearingen, J.D. and Blackwelder, R.F., 1987. "The growth and breakdown of streamwise vortices in the presence of a wall". *Journal of Fluid Mechanics*, Vol. 182, pp. 255–290.

Vinicius, M., Souza, L. and J. Liu, T.C., 2013. "Influence of Goertler Vortices Spanwise Wavelength on Heat Transfer Rates". *Computational Thermal Sciences: An International Journal*, Vol. 5, pp. 389–400.

Wang, H.P., Olson, S.J., Goldstein, R.J. and Eckert, E.R.G., 1997. "Flow Visualization in Linear Turbine Cascade of High Performance Turbine Blades". *ASME J. Turbomach.*, Vol. 19, pp. 01–08.

Zhang, D.H., Winoto, S.H. and Chew, Y.T., 1995. "Measurement in laminar and transitional boundary-layer flows on concave surface". *International Journal of Heat and Fluid Flow*, Vol. 16, pp. 88–98.

8. RESPONSIBILITY NOTICE

The following text, properly adapted to the number of authors, must be included in the last section of the paper:
The author(s) is (are) the only responsible for the printed material included in this paper.